Three-dimensional resolution-enhancement divided aperture correlation-differential confocal microscopy with nanometer axial focusing capability

LIRONG QIU,[1] YUN WANG,[1] HANXU WU,[1] YINGBIN SUN,[1] HAN CUI,[1,2] AND WEIQIAN ZHAO,[1,*] LIANG YUAN,[1,3] CHUNLIAN ZHAN[3]

[1]*Beijing Key Lab for Precision Optoelectronic Measurement Instrument and Technology, School of Optics and Photonics, Beijing Institute of Technology, Beijing 100081, China*
[2]*Division of Biomedical Engineering, School of Engineering, University of Glasgow, Glasgow G12 8LT, United Kingdom*
[3]*XI'AN Institute of Applied Optics, Xi'an 710065, China*
*zwq669@126.com

Abstract: Divided aperture confocal microscopy (DACM) provides an improved imaging depth, imaging contrast, and working distance at the expense of spatial resolution. Here, we present a new method-divided aperture correlation-differential confocal microscopy (DACDCM) to improve the DACM resolution and the focusing capability, without changing the DACM configuration. DACDCM divides the DACM image spot into two round regions symmetrical about the optical axis. Then the light intensity signals received simultaneously from two round regions by a charge-coupled device (CCD) are processed by correlation manipulation and differential subtraction to improve the DACM spatial resolution and axial focusing capability, respectively. Theoretical analysis and preliminary experiments indicate that, for the excitation wavelength of λ=632.8 nm, numerical aperture NA=0.8, and normalized offset v_M=3.2 of the two regions, the DACDCM resolution is improved by 32.5% and 43.1% in the x and z directions, simultaneously, compared with that of the DACM. The axial focusing resolution used for the sample surface profile imaging was also significantly improved to 2 nm.

References and links

1. G. J. Brakenhoff, H. T. M. van der Voort, E. A. Van Spronsen, W. A. M. Linnenans, and N. Nanninga, "Three-dimensional chromatin distribution in neuroblastoma nuclei shown by confocal scanning laser microscopy," Nature **317**, 748-749 (1985).
2. J.G. White and W. B Amos, "Confocal microscopy comes of age," Nature **328**,183-184 (1987).
3. A. E. Dixon, S. Danaskinos and M. R. Atkinson, "A scanning confocal microscope for transmission and reflecting imaging," Nature **351**, 551-553 (1991).
4. G. J. Puppels, F. F. M. de Mul, C. Otto, J. Greve, M. Robert-Nicoud, D. J. Arnd-Jovin and T. M. Jovin, "Studying single living cells and chromosomes by confocal Raman microspectroscopy," Nature **347**, 301-303 (1990).
5. Giuliano Scarcelli and Seok Hyun Yun, "Confocal Brillouin Microscopy for Three-dimensional Mechanical Imaging," Nat. Photonics **2**, 39-43 (2008).
6. Stefan W Hell, Steffen J Sahl, Mark Bates, Xiaowei Zhuang, Rainer Heintzmann, Martin J Booth, Joerg Bewersdorf, Gleb Shtengel, Harald Hess, Philip Tinnefeld, Alf Honigmann, Stefan Jakobs, IlariaTesta, Laurent Cognet, BrahimLounis, HelgeEwers, Simon J Davis, Christian Eggeling, David Klenerman, Katrin I Willig, Giuseppe Vicidomini, Marco Castello, Alberto Diaspro and Thorben Cordes, "The 2015 super-resolution microscopy roadmap," J. Phys. D: Appl. Phys. **48**, 443001(2015).
7. Udo Birk1, Johann v. Hase4, Christoph Cremer, "Super-resolution microscopy with very large working distance by means of distributed aperture illumination," Sci. Rep. **7**, 1-7(2017).
8. Koester, C.J., "Scanning mirror microscope with optical sectioning characteristics: applications in ophthalmology," Appl. Opt. **19**, 1749-1757 (1980).

9. Sheppard, C. and D. Hamilton, "High resolution stereoscopic imaging," Appl. Opt. **22**, 886-887 (1983).
10. Colin J. R. Sheppard, Wei Gong, and Ke Si, "The divided aperture technique for microscopy through scattering media," Opt. Express **16**, 17031-17038 (2008).
11. Wei Gong, Ke Si and Colin J. R. Sheppard, "Optimization of axial resolution in a confocal microscope with D-shaped apertures," Appl. Opt. **48**, 3998-4002 (2009).
12. Wei Gong, KeSi, and Colin J. R. Sheppard, "Divided-aperture technique for fluorescence confocal microscopy through scattering media," Appl. Opt. **49**, 752-757 (2010).
13. Charles J. Koester, Shyam M. Khanna, Heinz D. Rosskothen, Robert B. Tackaberry, and Mats Ulfendahl, "Confocal slit divided-aperture microscope: applications in ear research," Appl. Opt. **33**, 702-708 (1994).
14. J.F. Aguilar, "Confocal profiling of grooves and ridges with circular section using the divided aperture technique," Rev. Mex. Fis. **51**, 420–425 (2005).
15. Shuhao Shen, BinzhaoZhu, Yao Zheng, Wei Gong, and Ke SI, "Stripe-shaped apertures in confocal microscopy," Appl. Opt. **55**, 7613-7618 (2016).
16. Ye Ma, Cuifang Kuang, Wei Gong, Li Xue, Yao Zheng, Yifan Wang, Ke Si, and Xu Liu, "Improvements of axial resolution in confocal microscopy with fan-shaped apertures," Appl. Opt. **54**, 1354-1361 (2015).
17. E. H. K. Stelzer and S. Lindek, "Fundamental reduction of the observation volume in far-field light microscopy by detection orthogonal to the illumination axis: confocal theta microscopy," Opt. Commun. **111**, 536-547 (1994).
18. Lindek, S., C. Cremer, and E.H.K. Stelzer, "Confocal theta fluorescence microscopy with annular apertures," Appl. Opt. **35**, 126-130 (1996).
19. P. J. Dwyer, C. A. DiMarzio, J. M. Zavislan, "Confocal reflectance theta line scanning microscope for imaging human skin in vivo," Opt. Lett. **31**, 942-944 (2006).
20. Peter J. Dwyer, Charles A. DiMarzio, and M. Rajadhyaksha, "Confocal theta line-scanning microscope for imaging human tissues," Appl. Opt.**46**, 1843-1851 (2007)
21. T. Wang, M. Mandella, C. H. Contag, C. H. Contag, G. S. Kino, "Dual-axis confocal microscope for high-resolution in vivo imaging," Opt. Lett. **28**, 414-416 (2003).
22. L. K. Wong, M. J. Mandella, G. S. Kino, and T. D. Wang, "Improved rejection of multiply scattered photons in confocal microscopy using dual-axes architecture," Opt. Lett. **32**, 1674-1676 (2007).
23. HyejunRa, Wibool Piyawattanametha, Michael J. Mandella1, Pei-Lin Hsiung, Jonathan Hardy, Thomas D. Wang, Christopher H. Contag, Gordon S. Kino1, and O. Solgaard1, "Three-dimensional in vivo imaging by a handheld dual-axes confocal microscope," Opt. Express **16**, 7224-7232 (2008).
24. S. Y. Leigh and J. T. C. Liu, "Multi-color miniature dual-axis confocal microscope for point-of-care pathology," Opt.Lett. **37**, 2430-2432 (2012).
25. D. Wang, Y. Chen, Y. Wang, and J. T. C. Liu, "Comparison of line-scanned and point-scanned dual-axis confocal microscope performance," Opt.Lett. **38**, 5280-5283 (2013).
26. D. Wang, D. Meza,Y. Wang,L. Gao, and J. T. C. Liu, "Sheet-scanned dual-axis confocal microscopy using Richardson–Lucy deconvolution," Opt. Lett. **39**, 5431-5434 (2014).
27. D. S. Simon and A. V. Sergienko, "The correlation confocal microscope," Opt. Express **18**, 9765-9779 (2010).
28. O. Schwartz and D. Oron, "Improved resolution in fluorescence microscopy using quantum correlations," Phys. Rev. A **85**, 033812 (2012).
29. K. Si, W. Gong, C. J. R. Sheppard, "Three-dimensional coherent transfer function for a confocal microscope with two D-shaped pupils," Appl. Opt. **48**, 810-817 (2009)
30. C. J. Sheppard, W. Gong, and K. Si, "The divided aperture technique for microscopy through scattering media," Opt. Express **16**, 17031-17038 (2008).
31. Gong, W., K. Si, and C.J.R. Sheppard, "Improvements in confocal microscopy imaging using serrated divided apertures," Optics Com. **282**, 3846-3849(2009).
32. W. Gong, K. Si, and C. J. R. Sheppard, "Divided-aperture technique for fluorescence confocal microscopy through scattering media," Appl. Opt. **49**,752-757 (2010).

1. Introduction

A confocal microscope (CM) is an important tool in various scientific disciplines including physics, chemistry, biomedicine, and materials science due to its unique capabilities of optical sectioning and high spatial resolution imaging [1-6]. However, a conventional CM achieves high-resolution three-dimensional (3D) imaging through a high numerical aperture (NA) objective, resulting in a limitation of the imaged section depth to tens of microns. Therefore, CM can only be used for high-resolution 3D observations measurements on thin samples [7], and has the disadvantages of short working distance and low anti-scattering capabilities. Furthermore, the sample drift due to the long time-consuming scanning method of the point-by-point and layer-by-layer mode has a prominent effect on the CM imaging quality. These abovementioned problems prevent the use of the CM for samples that require a large field of view and large working distance, and have a strong scattering property.

In general, it is difficult to simultaneously improve the imaging resolution, sectioning depth discrimination, and working distance of a CM. For example, increasing the NA of the CM objective can improve the spatial resolution at the expense of the sectioning depth and working distance of CM. Therefore, the simultaneous improvement of these three parameters is an important issue that needs to be addressed.

To improve the field of view, optical section depth, and anti-scattering capability of a CM, a confocal microscopy imaging method based on the symmetrical lateral offset illumination and lateral offset detection has been proposed [8]. Using this method, divided aperture confocal microscopy (DACM) [9-16], confocal theta microscopy (CTM) [17-20], and dual-axis confocal microscopy (DCM) [21-26] have been developed for different requirements.

DACM partially shields the illumination and detection paths and improves the point spread function (PSF) of the microscope by using semicircular pupils in both the illumination and detection paths, thus enhancing the optical sectioning and anti-scattering capabilities [9-15]. Typical divided-aperture techniques used in DACM include D-shaped pupils [9-12], slit divided apertures [14], stripe-shaped apertures, and fan-shaped apertures [16]. In CTM, the illumination and detection axes are arranged at an angle θ and the PSF is optimized by reconstructing the spatial positions of the illumination and detection PSFs, improving the axial sectioning discrimination of CM [17]. Typical techniques include annular pupil confocal theta microscopy [18] and confocal theta line-scanning microscopy [19,20]. Based on CTM, DCM uses a low-NA and long working distance objective for illumination and detection to simultaneously achieve the long working distance, large field of view, and high axial resolution [21-26] , that makes it possible for the miniaturization of confocal microscopy systems. Hyejun Ra integrated a two-dimensional micro-electromechanical systems (MEMS) scanner into a long-working-distance DCM system, combined with an integrated optical system using a reflecting parabolic mirror for illumination and detection to develop a handheld dual-axes CM [23]. Steven Y. Leigh et al. combined the gradient index (GRIN) technology with a DCM system to develop a multicolor miniature dual-axis confocal microscope [24]. D. Wang et al. employed the cylindrical lens in the illumination path and line scanning detection technique in a DCM system and further developed a line-scanned dual-axis confocal microscope (LS-DACM) with an improved imaging speed [25]. However, the improvements in sectioning ability and working distance of DACM, CTM, and DCM were achieved at the expense of lateral resolution [8-11], which resulted in the decrease of the spatial resolution. The decrease in the spatial resolution, in turn, restricts the application of DACM, CTM, and DCM for high-spatial-resolution microscopic imaging fields. The improvement of the spatial resolution of confocal microscope is, therefore, a current issue of research in the field of optical microscopy imaging [6, 7, 27, 28].

Therefore, new imaging method-divided aperture correlation-differential confocal microscopy (DACDCM) is proposed to simultaneously improve the spatial resolution and axial focusing capability of DACM. Based on our discovered property that the slight lateral off-axis offset of the point detector in the DACM focal plane results in a shift of its axial intensity response curve, DACDCM divides the DACM image spot into two round regions symmetrical about the optical axis. The light intensity signals are then simultaneously received from the two round regions by a CCD and are processed by correlation manipulation and differential subtraction to improve the DACM spatial resolution and axial focusing capability, respectively. Therefore the spatial resolution and sample focusing capability of DACM was improved.

2. Principles

According to Fig. 1, the measurement principle of DACDCM is described as follows. In a DACM imaging system shown in Fig. 1(a), two virtual round detectors are symmetrically

placed with lateral offset M from the optical axis z_d, and the light intensity response $I(x, y, z, v_M)$ detected by DACM is given by [29-32]:

$$I(x,y,z,v_M) = \left| h_i(x,y,z) \times h_c(x,y,z,v_M) \right|^2$$

$$= \left| \frac{2\pi J_1(v_i)}{v_i} \right|^2 \times \left| \iint_{CA} P_c(\xi,\eta) \exp\left\{ i\left[(v_{cx}+v_M)\xi + v_{cy}\eta \right] \right\} d\xi d\eta \right|^2 \tag{1}$$

Here, J_1 is the first order Bessel function, $v_i^2 = v_{ix}^2 + v_{iy}^2$, ξ and η are the normalized coordinates in the pupil plane of the objective L_o, $P_i(\xi,\eta)$ is the illumination pupil function, $P_c(\xi,\eta)$ is the detection pupil function, v_M is the normalized optical offset of the detector lateral off-axis offset M expressed as $v_M = 2\pi MrR/(\lambda \times f_c)$, (v_{ix}, v_{iy}, u_i) are the normalized optical coordinates of (x_i, y_i, z_i), and (v_{cx}, v_{cy}, u_c) are the normalized optical coordinates of (x_c, y_c, z_c). The normalized optical coordinates and the coordinates (x, y, z) of DACM satisfy Eqs. (2) and (3):

$$\begin{cases} v_{ix} = \frac{2\pi}{\lambda} \cdot \sin\left[\arctan\left(\frac{r \cdot R}{f_o} \right) \right]\left[x\cos\left[\arctan\left(\frac{l \cdot R}{f_o} \right) \right] - z\sin\left[\arctan\left(\frac{l \cdot R}{f_o} \right) \right] \right] \\ v_{iy} = \frac{2\pi}{\lambda} \cdot \sin\left[\arctan\left(\frac{r \cdot R}{f_o} \right) \right] y \\ u_i = \frac{8\pi}{\lambda} \cdot \sin^2\left[\frac{1}{2} \cdot \arctan\left(\frac{r \cdot R}{f_o} \right) \right]\left[x\sin\left[\arctan\left(\frac{l \cdot R}{f_o} \right) \right] + z\cos\left[\arctan\left(\frac{l \cdot R}{f_o} \right) \right] \right] \end{cases} \tag{2}$$

$$\begin{cases} v_{cx} = \frac{2\pi}{\lambda} \cdot \sin\left[\arctan\left(\frac{r \cdot R}{f_o} \right) \right]\left[x\cos\left[\arctan\left(\frac{l \cdot R}{f_o} \right) \right] + z\sin\left[\arctan\left(\frac{l \cdot R}{f_o} \right) \right] \right] \\ v_{cy} = \frac{2\pi}{\lambda} \cdot \sin\left[\arctan\left(\frac{r \cdot R}{f_o} \right) \right] y \\ u_c = \frac{8\pi}{\lambda} \cdot \sin^2\left[\frac{1}{2} \cdot \arctan\left(\frac{r \cdot R}{f_o} \right) \right]\left[-x\sin\left[\arctan\left(\frac{l \cdot R}{f_o} \right) \right] + z\cos\left[\arctan\left(\frac{l \cdot R}{f_o} \right) \right] \right] \end{cases} \tag{3}$$

where, λ is the wavelength of the light source, r is the normalized radius of the illumination and detection pupils relative to the objective pupil, l is the normalized offset of the illumination and detection axis relative to the optical axis of the DACM system, R is the pupil radius of the objective L_o, f_o is the object focal length of the objective L_o, and f_c is the image focal length of the objective L_o.
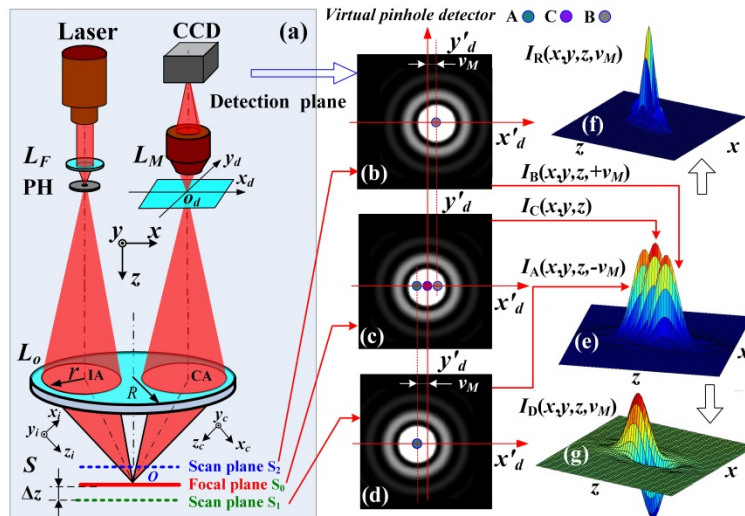

Fig. 1. Schematic of a DACDCM. (a) The DACM image principle. (b)-(d) the respective Airy spot pattern received by the CCD when the sample S is on the out-of- focal plane S_2, focal

plane S_0, and out-of- focal plane S_1. (e) Three intensity curves $I_A(x,y,z,-v_M)$, $I_C(x,y,z)$, and $I_B(x,y,z,+v_M)$. (f) The correlation intensity detection curve $I_R(x,y,z,v_M)$. (g) The differential intensity detection curve $I_D(x,y,z,v_M)$. Where (x, y, z) are the DACM system coordinates, (x_i, y_i, z_i) are the coordinates in the illumination space, and (x_c, y_c, z_c) are the coordinates in the detection space.

The DACM image principle is shown in Fig. 1(a), the beam emitted from the laser source is focused by the converging lens L_F, and then it passes through the pinhole PH and is focused on the test sample by the objective L_o. The reflected beam containing the measured information is focused by the objective L_o on the image point O_d, and the Airy spot at point O_d is magnified by the relay magnifier L_M before being detected by the CCD, and then three virtual round detectors A, B, and C were set by the measurement software on the Airy spot received by CCD, as shown in Fig. 1(c). Where the pinhole PH, object point O, and detector point O_d are conjugate. As shown Fig. 1(a), when the sample S moves along axis z, Fig. 1(e) shows three intensity curves $I_A(x,y,z,-v_M)$, $I_C(x,y,z)$, and $I_B(x,y,z,+v_M)$ received by the divided spot detection shown in Fig. 1(c), and when the sample S is on the out-of- focal plane S_2, focal plane S_0, and out-of- focal plane S_1, the respective Airy spot pattern received by the CCD are shown in Figs. 1(b)-1(d). Figure 1(f) shows the intensity detection curve $I_R(x,y,z,v_M)$ obtained by the correlation product processing of two intensity signals $I_A(x,y,z,-v_M)$ and $I_B(x,y,z,+v_M)$, and Fig. 1(g) shows the intensity detection curve $I_D(x,y,z,v_M)$ obtained by the differential subtraction of two intensity signals $I_A(x,y,z,-v_M)$ and $I_B(x,y,z,+v_M)$.

Assuming that the excitation wavelength of the DACM system is λ=632.8 nm, object focal length of L_o is f_o=1.8 mm, numerical aperture of L_o is NA = 0.8, pupil radius of L_o is R = 2.4 mm, $l = r = 0.5$, and M=0, the 3D PSF of the DACM can then be obtained by Eqs. (1)-(3), and the normalized full width at half maximum (FWHM) of the 3D PSF is FWHM = 6.4.

In the Airy spot pattern shown in Fig. 1(c), three virtual round detectors A, B, and C were set at the positions in the half of maximum intensity and the center of the spot, i.e. v_M=-3.2, 3.2, and 0, respectively. Then, the intensity responses in the x-z plane received from the three virtual round detectors were simulated by Eqs.(1)-(3), as shown in Fig. 1(e).

It can be seen from Fig. 1(e) that when the virtual round detectors were placed with an offset M, from the optical axis z_d, of the DACM system in the Airy spot shown in Fig. 1(c), the two intensity response curves $I_A(x,y,z,-v_M)$ and $I_B(x,y,z,+v_M)$ received by the two virtual round detectors A and B were shifted from the intensity response curves $I_C(x,y,z)$ received by the virtual round detector C, and the shift was determined by the offset M, between the virtual detector and system optical axis. Moreover, Figs. 1(b)-1(d) showed that when the sample had a slight offset from the focal plane of the objective L_o, the light spot on the CCD detection plane had an off-axis movement along the x_d axis in the detection focal plane, as shown in Figs. 1(b)-1(d).

To improve the spatial resolution and axial focusing capability of the DACM, we processed two intensity response signals $I_A(x,y,z,-v_M)$ and $I_B(x,y,z,+v_M)$ received from the two virtual detectors A and B by correlation product and differential subtraction respectively, and the correlated intensity signal $I_R(x,y,z,v_M)$ and differential intensity signal $I_D(x,y,z,v_M)$ were obtained, as follows.

$$I_R(x,y,z,v_M) = I_A(x,y,z,-v_M) \times I_B(x,y,z,+v_M) \qquad (4)$$

$$I_D(x,y,z,v_M) = I_B(x,y,z,+v_M) - I_A(x,y,z,-v_M) \qquad (5)$$

where (x,y,z) is the coordinates of the DADCM system shown in Fig. 1

Figures 1(f) and 1(g) show the correlation product and differential response curves of DACDCM in the x-z plane for v_M= 3.2. As can be seen from Fig. 1(f), the width of the main lobe of the DACDCM intensity response curve $I_R(x,y,z,v_M)$ in the x-z plane decreased as a result of the multiplication. As can be seen from Fig. 1(g), the differential confocal response curve $I_D(x,y,z,v_M)$ had a positive and negative bipolar response.

Figure 2 shows the simulation curves of the DACDCM and DACM intensity response properties for the *x*- and *z*-axes, respectively. Figures 2(a) and 2(b) show the simulated lateral intensity response curves of DACDCM and DACM for the *x*-axis, Figs. 2(c) and 2(d) show the simulated axial intensity response curves of DACDCM and DACM for the *z*-axis, and Figs. 2 (e) and 2(f) show the simulated axial focusing response curves of DACDCM in the differential subtraction mode and DACM for the *z*-axis.

It can be seen from Fig. 2(b) that the FWHMs of the DACDCM and DACM lateral response curves for the *x*-axis are Δx_R=0.253 μm and Δx_C=0.455 μm, respectively, implying that the DACDCM lateral resolution along the *x*-axis was improved by 44% compared with the DACM lateral resolution.

Similarly, it can be seen from Fig. 2(d) that the FWHMs of the DACDCM and DACM axial response curves were Δz_R=0.612 μm and Δz_C=1.095 μm, respectively, implying that the DACDCM axial resolution in the *z*-axis was also improved by 44% compared with the DACM axial resolution.

As can be seen from Fig. 2(f), the zero point *O* of the DACDCM differential confocal curve $I_D(0,0,z,v_M)$ corresponded exactly to the focus point (*z*=0) of the DACDCM system, and the zero point was in the middle of the most sensitive linear segment of the differential confocal curves, so the zero point *O* and its linear segment near point *O* in the DACDCM system could be used for the high precise focusing and measurement on the sample surface. In comparison to the focusing process of the DACM using the peak of the "bell"-shaped axial intensity response curve $I_B(0,0,z,v_M=0)$, the DACDCM axial focusing and measurement capabilities were significantly improved due to the best sensitivity and linearity of the axial response curve $I_D(0,0,z,v_M)$ near the zero point.
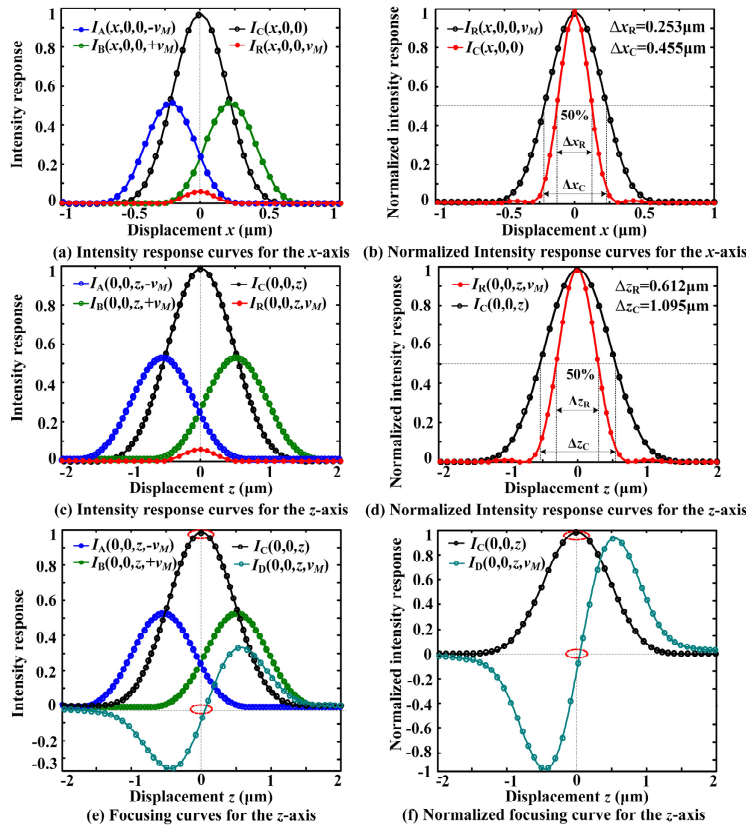

(a) Intensity response curves for the *x*-axis

(b) Normalized Intensity response curves for the *x*-axis

(c) Intensity response curves for the *z*-axis

(d) Normalized Intensity response curves for the *z*-axis

(e) Focusing curves for the *z*-axis

(f) Normalized focusing curve for the *z*-axis

Fig. 2. Simulations of the DACDCM and DACM intensity response properties. (a) Simulated intensity response of DACDCM and DACM in the *x*-direction. (b) Simulated normalized intensity response of DACDCM and DACM in the *x*-direction. (c) Simulated axial intensity response of DACDCM and DACM in the *z*-direction obtained through the simulation. (d) Simulated normalized axial intensity response of DACDCM and DACM in the z-direction. (e) Simulated axial focusing curves of DACDCM in the differential subtraction mode and DACM in the *z*-direction. (f) Simulated normalized axial focusing curves of DACDCM in the differential subtraction mode and DACM in the *z*-direction.

Therefore, it can be seen from Fig.2 that the theoretical resolution enhancement obtained through simulation are listed in Table 1, and DADCM can significantly enhance the DACM resolutions in the *x*- and *z*- directions.

Table 1. Theoretical resolution enhancement.

	x direction	*z* direction
FWHM of the DACM curve	0.455μm	1.095μm
FWHM of the DACDCM curve	0.253μm	0.612μm
Resolution enhancement	44%	44%

3. Experimental system and analysis

The above theory and simulation analysis showed that the DACDCM significantly improved the spatial resolution and axial focusing capability of DACM. To verify the effectiveness of DACDCM in improving the spatial resolution and axial focusing capability, we built an experimental setup based on the schematic shown in Fig. 1(a). In the experimental setup, a semiconductor laser (Thorlabs Inc. CPS180) with wavelength λ=632.8 nm was used as the light source, a CCD camera (WATEC 902H2 Ultimate) with 752 (H) × 582 (V) pixels and a unit cell size of 8.6 μm (H) × 8.3 μm (V) was used as the detector, a two-dimensional (2D) piezoelectric (PZT) ceramic nano-positioning system (PI Inc. P542) with a scanning feed resolution of 1 nm was used as the 2D lateral sample scanning stage, a piezoelectric ceramic nano-focusing z-driver (PI Inc. P725) with a driving resolution of 1.25 nm was used as the objective scanning system to scan the test sample along the *z*-axis; and a 100× long working distance flat field achromatic objective lens (OLYMPUS) with a focal length of f_o=1.8 mm, a numerical aperture of NA = 0.8, and a working distance of ~3.4 mm was used as the system objective L_o. The normalized offset *l* and the normalized radius *r* of the illumination and detection pupils were *l*=*r*=0.5, the image focal length of the objective L_o was f_c=150 mm, the magnification of the magnifier L_M was 10 times, and the diameter of the magnified image spot on the CCD was ~1608.4 μm. The diameters of the two virtual round detectors A and B set in the CCD image plane were 545 μm, the normalized lateral offset of the pinholes was v_M=3.2, and the corresponding actual offset was *M*=805 μm. In addition, to compare with the DACM system, a virtual round detector *C* without offset, representing the intensity response of the DACM system, was set in the CCD image plane.

To test the lateral resolution property of the DACDCM, we used the DACDCM and DACM systems to scan the straight edge of the glass substrate coated with a cobalt reflecting film along *x*-axis, and the measured step response curves of DACDCM and DACM are shown in Fig. 3(a), where the curves $I_A(x,0,0,-v_M)$, $I_C(x,0,0)$, and $I_B(x,0,0,+v_M)$ were the measured lateral response curves when the virtual round detectors A, C, and B were placed according to the positions in Fig. 1(c). The curve of $I_R(x,0,0,v_M)$ shown in Fig. 3(b) was obtained by correlation product of the measured curves $I_A(x,0,0,-v_M)$ and $I_B(x,0,0,+v_M)$. Here, we define the lateral interval corresponding to the normalized intensity from 0.2 to 0.8 as the rising edge widths of the step response curves, and the lateral resolution is better, the rising edge width is narrower. It can be seen from the measured normalized step response curves $I_R(x,0,0,v_M)$ and $I_C(x,0,0)$ shown in Fig. 3(b) that the rising edge widths of the step response curves for the DACDCM and DACM were $W(x_R)$ = 0.27 μm and $W(x_C)$ = 0.40 μm, respectively, and the lateral resolution of the DACDCM was improved by 32.5%, better than that of the DACM, which was in agreement with the simulation results shown in Fig. 2(b).
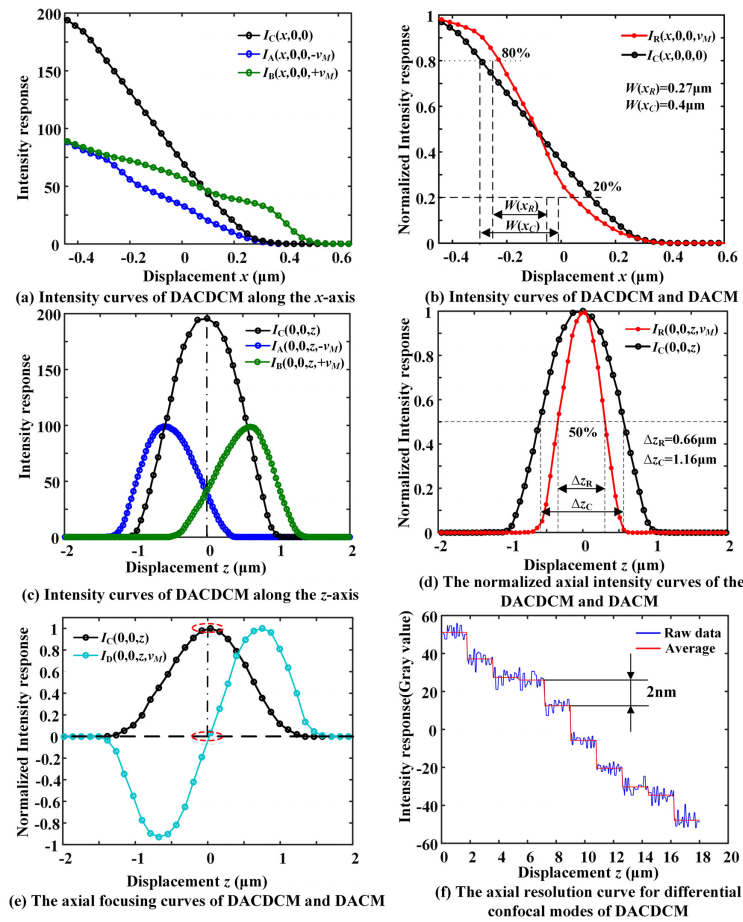
Fig. 3. Measured intensity response and axial focusing curves of the DACDCM and DACM. (a) Measured intensity response of DACDCM and DACM in the *x*-direction. (b) Measured normalized intensity response of DACDCM and DACM in the *x*-direction. (c) Measured axial intensity response of DACDCM and DACM in the *z*-direction. (d) Measured normalized axial intensity response of DACDCM and DACM in the *z*-direction. (e) Measured axial focusing curves of DACDCM in the differential subtraction mode and DACM in the *z*-direction. (f) Measured axial resolution curve of DACDCM in the differential subtraction mode.

To test the axial resolution property of the DACDCM, we used the DACDCM and DACM systems to scan a flat glass sample coated with silver reflecting film along the optical axis, and the measured axial response curves of DACDCM and DACM are shown in Fig. 3(c), where curves $I_A(0,0,z,-v_M)$, $I_C(0,0,z)$, and $I_B(0,0,z,+v_M)$ are the measured axial response curves when the virtual round detectors A, C and B were placed according to the positions in Fig. 1(c). The curves of $I_D(0,0,z,-v_M)$ shown in Fig. 3(d) was obtained by correlation product of the measured curves $I_A(0,0,z,-v_M)$ and $I_B(0,0,z,+v_M)$, and it can be seen from the measured normalized step response curves $I_R(x,0,0,v_M)$ and $I_C(x,0,0)$ that the respective FWHMs of the axial response curves $I_R(x,0,0,v_M)$ and $I_C(x,0,0)$ were Δz_R=0.48 μm and Δz_C=0.79 μm. The axial resolution of DACDCM was improved by 43.1%, better than that of DACM, which was in agreement with the simulation results shown in Fig. 2(d).

To demonstrate the axial focusing capability of DACDCM, we used the DACDCM and DACM to scan a flat glass sample coated with silver reflecting film along the optical axis. The measured axial response curves are shown in Fig. 3(e), where the curves $I_A(0,0,z,-v_M)$, $I_C(0,0,z)$, and $I_B(0,0,z,+v_M)$ are the measured axial intensity curves when the virtual round

detectors A, C, and B were placed according to the positions in Fig. 1(c). The curve $I_D(0,0,z,v_M)$ was obtained by the subtraction of curves $I_A(0,0,z,-v_M)$ and $I_B(0,0,z,+v_M)$, and it can be seen from Fig. 3(e) that the measured curves $I_D(0,0,z,v_M)$ and $I_C(0,0,z)$ were in agreement with the theoretical simulation results shown in Fig. 2(f). Figure 3(f) shows the actual axial resolution curve measured by the differential confocal curve $I_D(0,0,z,v_M)$ when the nanometer-precision objective scanning system moved with 2 nm axial feed steps. And as can be seen from this, the DACDCM could clearly discriminate the sample with a 2-nm axial feed, so the axial resolution for differential confocal modes was better than 2 nm.

Therefore, it can be seen from Fig. 3 that the measured resolution enhancement are listed in Table 2, and DADCM significantly enhance the DACM resolutions in the x- and z-directions.

Table 2. Measured resolution enhancement.

	x direction	z direction
Axial FWHM and lateral edge rising width of the DACM curve	0.40μm	1.16μm
Axial FWHM and lateral edge rising width of the DACDCM curve	0.27μm	0.66μm
Resolution enhancement	32.5%	43.1%

To further verify the 3D image capability of DACDCM, we used atomic force microscopy (AFM), DACDCM, and DACM to measure the 3D profiles of the standard step samples with nominal heights of 20 nm and 100 nm, respectively. Since the lateral and axial resolutions of AFM were both better than 1 nm, the step profile measured by AFM can be used as the standard value, and the differences between the profile values measured by DACDCM and DACM, and the standard profile measured by AFM were used to verify the effects of DACDCM on improving 3D imaging capability of DACM.

Here, DADCM has two axial scanning modes of sectioning and sensing. When the thickness of the measured sample is larger than the linear range of DADCM axial response curve, DADCM measures the sample using the sectioning scanning mode, and otherwise it measures the sample using the sensing mode. For the 100-nm height sample, the scanning parameters are the lateral scanning step of 80 nm, the frame images of 128×32 in a lateral section, the axial scanning interval of 100 nm, and the axial scanning layer of 40. So, CCD frames of 163840 are measured to obtain the surface topography of 100-nm height sample, shown in Fig. 4. For the 20-nm height sample, the scanning parameters are the lateral scanning step of 100 nm, the frame images of 128×32 in a lateral section, and the lateral profile is obtained by DADCM axial differential curve in a section. So, CCD frames of 4096 are measured to obtain the surface topography of 20-nm height sample, as shown in Fig. 4.

When DACM measures the height samples of 20-nm and 100-nm, it used the fitted maximum to measure the surface topography, so it needs the scanning in the both lateral (x and y) and axial directions. Here, the scanning parameters are the lateral scanning step of 100 nm and the frame images of 128×32 in a lateral section. The axial scanning intervals are 50 nm for the 100-nm height sample and 10 nm for the 20-nm height sample, and the axial scanning layers are 40 layers for the 100-nm height sample and 100 layers for the 20-nm height sample, as shown in Fig. 4.
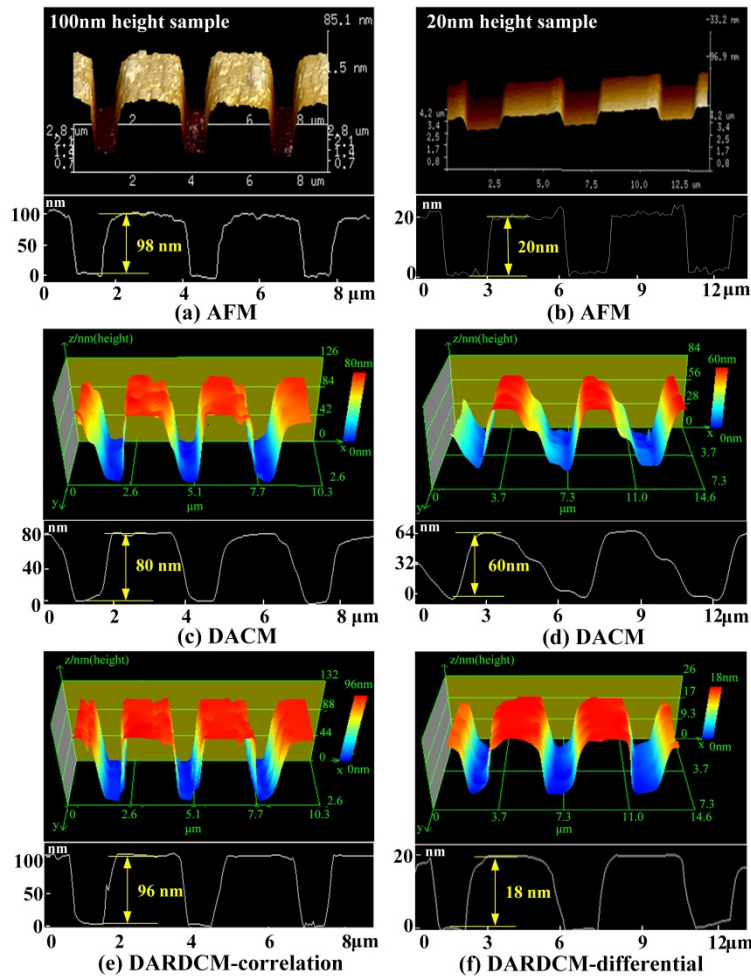
Fig. 4. 3D profile of the step measured by AFM, DACM, and DACDCM. (a) Profile of the step with 100-nm height measured by AFM. (b) Profile of the step with 20-nm height measured by AFM. (c) Profile of the step with 100-nm height measured by DACM. (d) Profile of the step with 20-nm height measured by DACM. (e) Profile of the step with 100-nm height measured by DACDCM. (f) Profile of the step with 20-nm height measured by DACDCM. In which, the color bar represents the measured height and it is able to adaptive height change.

Figure 4 shows the 3D profiles, 2D profiles, and step height of the standard step sample, which were measured by AFM, DACDCM, and DACM. Figs. 4(c) and 4(d) show the profiles of the step sample with heights of 100nm and 20 nm, measured by a point-by-point and layer-by layer scan with the extreme point of the DACM intensity curve $I_C(x,y,z)$. Figures 4(e) and 4(f) show the profiles of the step sample with heights of 100 nm and 20 nm, which were measured by a point-by-point and layer-by layer scan with the extreme point of correlation property curve $I_R(x,y,z,v_M)$ of DACDCM. As can be seen from Figs. 4(a), 4(c) and 4(e), the step heights measured by AFM, DACM, and DACDCM were H_A=98 nm, H_C=80 nm, and H_R= 96 nm, respectively. The difference in the step height measured by DACDCM and AFM was only 2 nm, but the difference in the step height measured by DACM and AFM was 18 nm. Therefore, the DACDCM significantly improved the axial resolution of the DACM. Moreover, the shape of the step profile measured by DACDCM was close to that measured by AFM, but the shape of the step profile measured by DACM had obvious differences from that measured

by AFM, and there was a strong distortion in the cross section of the step. Therefore, DACDCM significantly improved the lateral resolution of DACM.

As can be seen from Figs. 4(b), 4(d) and 4(f), the step height measured by AFM, DACM, and DACDCM were H_A=20 nm, H_C=62 nm, and H_R=18 nm, respectively, and the difference in step height measured by DACDCM and AFM was only 2 nm, but the difference of the step height measured by DACM and AFM was 40 nm, which was a measurement mistake. Therefore the differential subtraction mode of DACDCM significantly improved the axial resolution and axial focusing capability of the DACM. Moreover, DACDCM also significantly improved the speed of the measurement when the DACDCM was in the differential subtraction mode using the linear segment of the differential curve $I_D(x,y,z,v_M)$ to measure the 3D profile of the height step sample by direct single layer scanning.

4. Conclusions

We found that the lateral offset of the detector caused a shift of the axial intensity response curve in DACM. Based on this feature, we proposed a 3D high-resolution DACDCM method with an axial focusing capability at the nanometer scale. Theoretical analysis and experiments indicated that the DACDCM improved the lateral and axial resolutions of the DACM by 32.5% and 43.1%, respectively, when DACDCM and DACM had the same configuration, and the axial focusing resolution was significantly improved to 2 nm. Moreover, the differential confocal measurement mode of DACDCM was used to directly achieve the 3D profile measurement with nanometer precision by single layer fast scanning. Therefore, DACDCM provides a novel approach in the improvement of the DACM spatial resolution and axial focusing capability.

Funding